

# Resolved HI in two ultra–diffuse galaxies from contrasting non-cluster environments

T. C. Scott<sup>1</sup>\*, Chandreyee Sengupta,<sup>2</sup> P. Lagos<sup>1</sup>, Aeree Chung<sup>3</sup>, O. Ivy Wong<sup>4,5,6</sup>

<sup>1</sup> *Institute of Astrophysics and Space Sciences (IA), Rua das Estrelas, 4150-762 Porto, Portugal*

<sup>2</sup> *Purple Mountain Observatory, No.8 Yuanhua Road, Qixia District, Nanjing 210034, China*

<sup>3</sup> *Department of Astronomy, Yonsei University, 50 Yonsei-ro, Seodaemun-gu, Seoul, Republic of Korea*

<sup>4</sup> *CSIRO Astronomy & Space Science, PO Box 1130, Bentley, WA 6102, Australia*

<sup>5</sup> *ICRAR-M468, University of Western Australia, Crawley, WA 6009, Australia*

<sup>6</sup> *ARC Centre of Excellence for All Sky Astrophysics in 3 Dimensions (ASTRO 3D), Australia*

## ABSTRACT

We report on the first resolved HI observations of two blue ultra-diffuse galaxies (UDGs) using the Giant Metrewave Radio Telescope (GMRT). These observations add to the so-far limited number of UDGs with resolved HI data. The targets are from contrasting non-cluster environments: UDG–B1 is projected in the outskirts of Hickson Compact Group 25 and Secco–dI–2 (SdI–2) is an isolated UDG. These UDGs also have contrasting effective radii with  $R_e$  of 3.7 kpc (similar to the Milky Way) and 1.3 kpc respectively. SdI–2 has an unusually large  $\frac{M_{HI}}{M_*}$  ratio = 28.9, confirming a previous single dish HI observation. Both galaxies display HI morphological and kinematic signatures consistent with a recent tidal interaction, which is also supported by observations from other wavelengths, including optical spectroscopy. Within the limits of the observations’ resolution our analysis indicates that SdI–2 is dark matter-dominated within its HI radius and this is also likely to be the case for UDG–B1. Our study highlights the importance of high spatial and spectral resolution HI observations for the study of the dark matter properties of UDGs.

**Key words:** galaxies: individual: UDG–B1 and Secco–dI–2 – galaxies: ISM – galaxies: interactions – galaxies: kinematics and dynamics – radio lines: galaxies

## 1 INTRODUCTION

Recent studies (van Dokkum et al. 2015; Koda et al. 2015; Yagi et al. 2016) have reported over 1000 extended diffuse galaxies in and surrounding the Coma galaxy cluster ( $z = 0.0231$ ). These galaxies have central surface brightnesses ( $\mu_g$ ) of  $\sim 24 - 26$  mag arcsec<sup>-2</sup>, effective radii<sup>1</sup> ( $R_e$ )  $\sim 1.5 - 5$  kpc, median stellar masses of  $\sim 6 \times 10^7 M_\odot$  and were designated by van Dokkum et al. (2015) as ultra–diffuse galaxies (UDGs). These UDGs have a median  $R_e$  similar to L\* spirals ( $R_e \sim 3.7$  kpc) but their median stellar masses are more typical of dwarf galaxies  $\sim 10^{7-8} M_\odot$  (Lagos et al. 2011, and references therein). While faint, extended, low surface brightness galaxies (LSBs) are not a recent discovery, the Coma UDGs reveal their higher abundance in dense environments (van der Burg et al. 2017). Compared to classical LSBs, UDGs are optically fainter and often more extended (Yagi et al. 2016) with a wide range of optical  $R_e$ . Conselice (2018), argues UDGs are part of an earlier reported population of Low–Mass Cluster Galaxies

(LMCGs) and attributes their large diameters to interactions with the cluster environment and expected them to be dark matter (DM) dominated. On the face of it, the reported tight correlation between the abundance of UDGs and the mass of the host clusters and groups (van der Burg et al. 2017; Román & Trujillo 2017) supports environmentally driven formation scenarios, such as those proposed by Baushev (2016); Yozin & Bekki (2015); Carleton et al. (2018). Janssens et al. (2019) reported on the abundance and distribution of UDGs in 6 massive clusters at  $z = 0.308$  to 0.545. The asymmetric distribution of UDG around 4 of the Janssens et al. (2019) clusters and the anticorrelation between the UDG and compact dwarf galaxy distributions highlights the likely role of the cluster environment in both the formation and evolution of UDGs. However, UDGs are also found in groups and in isolation which has led to alternative formation models which rely, to a greater or lesser extent, on secular processes, e.g. objects from the high–end tail of the DM halo spin parameter distribution (Amorisco & Loeb 2016) or star formation (SF) driven gas outflows generating extended discs and quenching SF (Di Cintio et al. 2017). Whether UDG/LMCGs (referred from here on as UDGs) turn out to be a subset of classical LSBs, as suggested by Tanoglidis et al. (2020), or separate class(es) of their own, is

\* tom.scott@astro.up.pt

<sup>1</sup> The effective radius of a galaxy is the radius at which half of the total light is emitted

likely to depend on the so-far unresolved question of how LSBs and UDGs form. Attention is turning toward the DM content and its distribution in UDGs because of its critical role in the formation and evolution of their observable baryonic components. Beyond the cluster environment, where significant ram pressure stripping of a UDGs H I is not expected, H I studies become feasible. Resolved H I in particular is well suited to both the detection of recent interactions and determination of DM properties and as a result, can assist in answering these questions.

In this paper, we present resolved Giant Metrewave Radio Telescope (GMRT) H I observations of two blue ( $g - i < 0.6$ ) UDGs from contrasting non-cluster environments; UDG–B1 is projected in the outskirts of Hickson Compact Group 25 (HCG 25) (Román & Trujillo 2017; Spekkens & Karunakaran 2018) while Secco–dI–2 (hereafter SdI–2) is a relatively isolated blue UDG (Bellazzini et al. 2017). Because of gas stripping in dense environments we would expect UDGs in those environments to have redder colours than the the  $g - i < 0.6$  colour predicted for UDGs in low density environments (Liao et al. 2019) and UDG–B1 is the bluest UDG ( $g - i = 0.27 \pm 0.05$ ) in a sample of bluer ( $0.27 < g - i < 0.55$ ) UDGs surrounding Hickson Compact groups from Román & Trujillo (2017). Table 1 gives a summary of the UDG–B1 and SdI–2 properties. There are differing definitions in the literature of a UDG, in particular, the criteria for their  $R_e$ , e.g. (Yagi et al. 2016,  $>0.7$  kpc), (Román & Trujillo 2017,  $>1.3$  kpc), although the van Dokkum et al. (2015) definition of  $>1.5$  kpc is widely used. SdI–2 ( $R_e = 1.3 \pm 0.1$ ) has previously been classified as a UDG by Bellazzini et al. (2017); Papastergis et al. (2017) and (Wang et al. 2020). But we note that while the SdI–2  $R_e$  is above the  $R_e$  of  $\sim 1$  kpc of local group dwarf galaxies (Guo et al. 2020) it is below the minimum  $R_e$  of 1.5 kpc for UDGs adopted by many authors, e.g. Forbes et al. (2020a) who would consider SdI–2 as a “small UDG” or “LSB dwarf” rather than a UDG. The  $R_e$  of SdI–2 lies only slightly below the  $R_e$  1.5 kpc, which is confirmed by the fact that its  $R_e$  lies within uncertainties of three of the UDGs in the Leisman et al. (2017) sample of HI rich UDGs. Additionally  $R_e$  measurement can change significantly with the optical band (Forbes et al. 2020b). SdI–2’s  $R_e$  (measured at  $1.3 \pm 0.1$  kpc in i band) may well be above 1.5 kpc in g band. Thus given its proximity to the strictest  $R_e$  lower limit and consistency with the previous classifications of SdI–2 as a UDG, we adopt its classification as a UDG. We use optical images from the Sloan Digital Sky Survey (SDSS), IAC Stripe 82 and Pan-STARRS1 (Flewelling et al. 2016) as well as UV imaging from Galaxy Evolution Explorer (GALEX) in this paper. UDG–B1 also has an SDSS spectrum that we utilise as part of our analysis.

Section 2 gives details of the GMRT observations, with observational results in section 3. A discussion follows in section 4 with a summary and concluding remarks in section 5. To aid comparisons in this paper we adopt distances to UDG–B1 and SdI–2 of 88 Mpc and 40 Mpc, respectively from Spekkens & Karunakaran (2018) and Papastergis et al. (2017). We also adopt their angular scales of 1 arcmin  $\sim 25$  kpc and 1 arcmin  $\sim 11$  kpc, for UDG–B1 and SdI–2, respectively. All  $\alpha$  and  $\delta$  positions referred to throughout this paper are J2000.0.

## 2 OBSERVATIONS

UDG–B1 and SdI–2 were observed in H I using the GMRT on 2018 March 8th and 9th and selected observational parameters are detailed in Table 2. H I in UDG–B1 has previously been detected

**Table 1.** Properties of UDG–B1 and SdI–2

Property <sup>a</sup>	Units	UDG–B1	SdI–2
$V_{optical}$ <sup>b</sup>	[km s <sup>−1</sup> ]	6445±12	2549±50
$V_{HI\ W20}$	[km s <sup>−1</sup> ]	<b>6450± 7</b>	<b>2565± 4</b>
$W_{W20}$	[km s <sup>−1</sup> ]	<b>90± 15</b>	<b>80± 6</b>
RA <sup>c</sup>	[h:m:s]	03 20 21.1	11 44 33.8
DEC	[d:m:s]	-01 10 12.0	-00 52 00.9
Distance <sup>d</sup>	[Mpc]	88	40±1
$R_e$ <sup>e</sup>	[kpc]	3.7±0.4	1.3±0.1
$\mu_g(0)$ <sup>f</sup>	[mag arcsec <sup>2</sup> ]	24.0	>24.0
Morphology		UDG	UDG
12+log(O/H) <sup>g</sup>		7.91± 0.32	8.1±0.2
$S_{HI}$ (GMRT)	[Jy km s <sup>−1</sup> ]	<b>0.8±0.04</b>	<b>0.69±0.03</b>
$M_{HI}$ (GMRT)	[10 <sup>8</sup> M <sub>⊙</sub> ]	<b>15</b>	<b>2.6</b>
$M_*$ <sup>h</sup>	[10 <sup>8</sup> M <sub>⊙</sub> ]	2.2±0.3	0.09
$g - i$ <sup>i</sup>		0.27± 0.05	0.19

<sup>a</sup> From the literature as noted or if in bold typeface from this work.

<sup>b</sup> SdI–2 from Bellazzini et al. (2017).

<sup>c</sup> RA and DEC positions for UDG–B1 are from Román & Trujillo (2017) and SdI–2 are from (Bellazzini et al. 2017).

<sup>d</sup> See section 1.

<sup>e</sup> UDG–B1 from Román & Trujillo (2017), SdI–2 from Bellazzini et al. (2017).

<sup>f</sup> UDG–B1 from Trujillo et al. (2017).

<sup>g</sup> For UDG–B1 from a SDSS spectrum of the brightest SF knot see Table 3 and SdI–2 from (Bellazzini et al. 2017).

<sup>h</sup> UDG–B1 from Román & Trujillo (2017), SdI–2 from Papastergis et al. (2017).

<sup>i</sup> UDG–B1 from Román & Trujillo (2017). SdI–2 from SDSS photometry.

within a VLA D–configuration field (Spekkens & Karunakaran 2018; Borthakur et al. 2010) centred on the HCG 25 group. The UDG–B1 H I was unresolved in the VLA 70 × 50 arcsec FWHM synthesised beam, which provided the motivation to reobserve UDG–B1 with the GMRT to obtain the first ever resolved mapping of its H I. The GMRT data was reduced and analyzed using the standard reduction procedures with the Astronomical Image Processing System (AIPS) software package. The flux densities are on the scale of Baars et al. (1977), with uncertainties of  $\sim 5\%$ . After calibration and continuum subtraction in the uv domain the AIPS, task IMAGR was used to convert the uv domain data to H I image cubes. Finally integrated H I and velocity field maps were extracted from the image cubes using the AIPS task MOMNT. To study the H I distribution in detail, image cubes with different resolutions were produced by applying different ‘tapers’ to the data with varying uv limits. Details of the final low, medium and high resolution maps are given in Table 2.

## 3 OBSERVATIONAL RESULTS

### 3.1 HI morphology and mass

UDG–B1 is projected  $\sim 9$  arcmin (225 kpc) SW of the Hickson Compact Group, HCG 25 centre, see Figure 1. The UDG’s heliocentric radial velocity ( $V_{opt}$ ) is 89 km s<sup>−1</sup> higher than the mean velocity for HCG 25,  $V_{opt} = 6356$  km s<sup>−1</sup> (NED) with a dispersion ( $\sigma_v$ ) = 61.3 km s<sup>−1</sup> (Tovmassian et al. 1999). UDG–B1 is projected within the typical group  $R_{200}$  of 500 kpc (Román & Trujillo 2017),

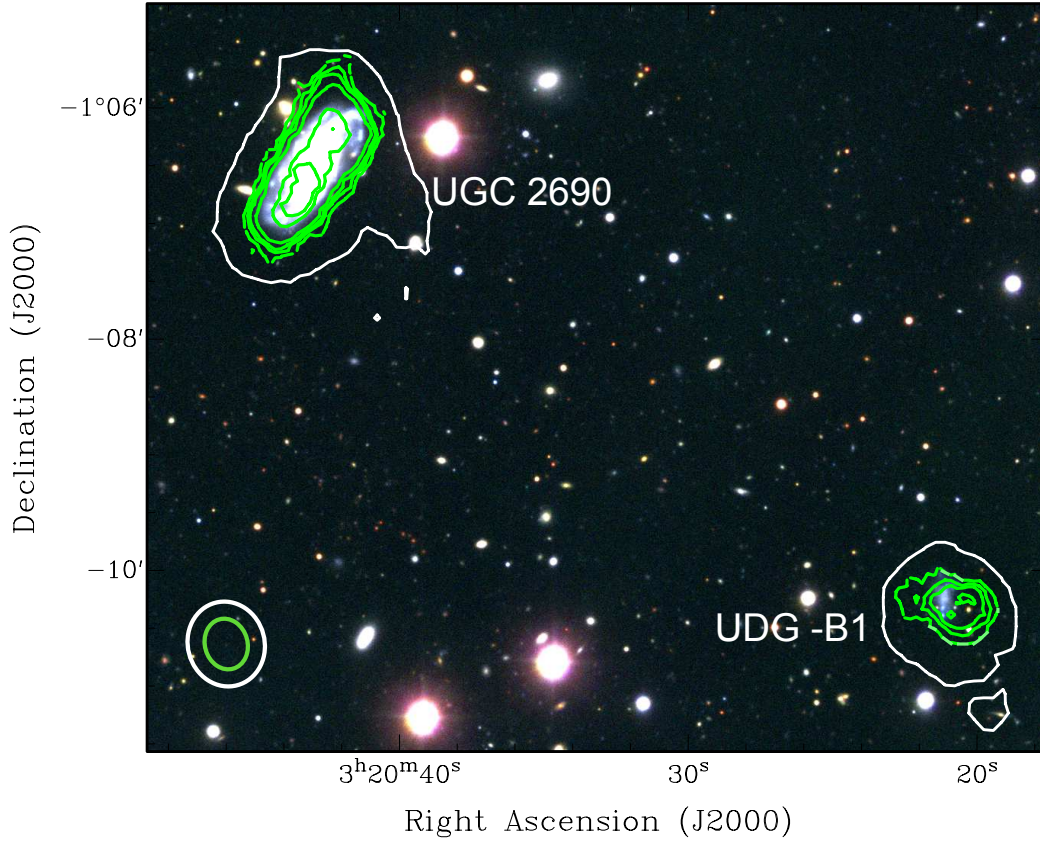


**Figure 1.** Wide-angle region SW of HCG 25 with the GMRT low resolution ( $44.82'' \times 40.48''$ ) H I contour (white) at  $0.39 \times 10^{20}$  atoms  $\text{cm}^{-2}$  and medium resolution ( $26.46'' \times 22.65''$ ) H I contours (green) at 1.46, 2.73, 3.6, 5.5 11.0 and  $13.8 \times 10^{20}$  atoms  $\text{cm}^{-2}$ . These contours are overlaid on an IAC stripe 82 composite g, r, i image showing H I detections in UGC 2690 and UDG-B1. The ellipses at the bottom left indicate the size and orientation of the GMRT synthesized beams.

where  $R_{200}$  is the radius enclosing an overdensity of  $> 200$  with respect to the critical density of the universe. Its projected position and velocity are therefore consistent with UDG-B1 being an outskirts member of HCG 25 so past interactions between the UDG-B1 and HCG 25 group members cannot be ruled out. H I was detected in UDG-B1 with the GMRT at a velocity<sup>2</sup> ( $V_{\text{HI}}$ ) =  $6450 \pm 7$   $\text{km s}^{-1}$  and in HCG 25 member UGC 2690 ( $V_{\text{opt}} = 6285$   $\text{km s}^{-1}$ ,  $W_{20} = 340 \pm 8$   $\text{km s}^{-1}$ ), projected 6.6 arcmin NE and within 165  $\text{km s}^{-1}$  of UDG-B1, see Figure 1. Further details of the H I detected in UGC 2690 are presented in Appendix A.

The left-hand panels of Figure 2 show (top to bottom) the low ( $44.82'' \times 40.48''$ ), medium ( $26.46'' \times 22.65''$ ) and high ( $22.73'' \times 15.31''$ ) resolution GMRT UDG-B1 integrated H I map contours overlaid on an IAC Stripe 82 g, r, i composite image. The high resolution H I map contours reveal significant asymmetry in the H I morphology, with the bulk of the high column density H I offset by  $\sim 20$  arcsec (8 kpc) from optical centre. For UGC-B1 the GMRT flux density ( $S_{\text{HI}}$ ) =  $0.8$   $\text{Jy km s}^{-1}$  which converts to an  $M_{\text{HI}} \sim 1.5 \times 10^9 M_{\odot}$ . Spekkens & Karunakaran (2018) have previously reported Green Bank Telescope (GBT) single dish and Very Large

Array (VLA) H I detections for UGC-B1 with  $S_{\text{HI}} = 0.6 \pm 0.1$   $\text{Jy km s}^{-1}$  from the VLA data. At the adopted distance of 88 Mpc this VLA  $S_{\text{HI}}$  implies  $M_{\text{HI}} = 1.1 \times 10^9 M_{\odot}$ , in good agreement with the  $M_{\text{HI}}$  derived from the GMRT. The VLA flux density sensitivity was  $\sim 0.5$   $\text{mJy beam}^{-1}$  (Borthakur et al. 2010), quite similar to GMRT medium and high resolution maps. For the GBT spectrum Spekkens & Karunakaran (2018) reported a higher peak signal to noise ratio (15.2) than from the VLA spectrum (9.2). At first sight this may seem like some flux loss for the interferometric observations. However, while the GBT pointing was at the position UDG-B1 the GBT FWHP beam is  $\sim 9$  arcmin and thus the spectrum was contaminated by emission from UGC 2690. UGC 2690 is projected 6.6 arcmin from UDG-B1, so lies just beyond the radius of GBT FWHP beam. Combining the GMRT H I spectra of UDG-B1 and UGC 2690, attenuated to 40% of its actual flux, produces a spectrum consistent with the GBT spectrum. So, for the analysis in this paper we adopt the GMRT H I mass. Based on this H I mass and the  $M_{*}$  from Table 2 the  $\frac{M_{\text{HI}}}{M_{*}}$  ratio for UGC-B1 is 6.8.

For SdI-2, Figure 3 (Top row) shows the low ( $39.95'' \times 35.38''$ ) and medium ( $24.50'' \times 21.99''$ ) resolution GMRT integrated H I map contours overlaid on a smoothed Pan-STARRS g, r, i composite image. Figure 3 shows the main body of the galaxy has an H I extent of  $\sim 1.2$  arcmin (13.6 kpc). A detached H I tail like

<sup>2</sup> The H I velocity was determined from the mid point in the  $W_{20}$  velocity range, i.e.  $V_{\text{HI } W_{20}}$  as defined in Reynolds et al. (2020).

**Table 2.** GMRT observational and map parameters

<b>UDG-B1</b>	
Rest frequency	1420.4057 MHz
Observation Date	2018 Mar 9
Integration time	10.0 hrs
primary beam	24' at 1420.4057 MHz
Low resolution beam–FWHP	44.82'' × 40.48'', PA = 14.03°
Medium resolution beam–FWHP	26.46'' × 22.65'', PA = 15.80°
High resolution beam–FWHP	22.73'' × 15.31'', PA = -9.61°
RA (pointing centre)	03 <sup>h</sup> 20 <sup>m</sup> 21.102 <sup>s</sup>
DEC (pointing centre)	-01° 10' 13.992''
<b>SdI-2</b>	
Rest frequency	1420.4057 MHz
Observation Date	2018 Mar 8
Integration time	10.0 hrs
primary beam	24' at 1420.4057 MHz
Low resolution beam–FWHP	39.95'' × 35.38'', PA = -10.63°
Medium resolution beam–FWHP	24.50'' × 21.99'', PA = 21.18°
RA (pointing centre)	11 <sup>h</sup> 44 <sup>m</sup> 33.802 <sup>s</sup>
DEC (pointing centre)	-00° 52' 00.913''

extension was also detected to the NE of the main H I body reaching  $\sim 2.4$  arcmin (26 kpc) NE of the optical centre in the medium resolution H I map. H I in this extended region has a column density maximum  $> 7 \times 10^{19}$  atoms  $\text{cm}^2$ . The main H I body of SdI-2 has optical, NUV and FUV (GALEX) and NIR (WISE 3.4  $\mu\text{m}$  and 4.6  $\mu\text{m}$ ) counterparts, see Figure 3 – Lower right panel. For SdI-2 the GMRT  $S_{\text{HI}} = 0.69 \pm 0.03$  J  $\text{km s}^{-1}$  which at the adopted distance of 40 Mpc gives  $M_{\text{HI}} \sim 2.6 \times 10^8 M_{\odot}$ . A previous H I detection for SdI-2 using the Effelsberg 100 m single dish telescope gave  $S_{\text{HI}} = 0.63$  Jy  $\text{km s}^{-1}$  which converts to  $M_{\text{HI}} = 2.4 \times 10^8 M_{\odot}$  (Papastergis et al. 2017), in good agreement with the  $M_{\text{HI}}$  derived from the GMRT. For the analysis in this paper we adopt the GMRT H I mass. Based on the GMRT H I mass and the  $M_*$  from (Papastergis et al. 2017), the  $\frac{M_{\text{HI}}}{M_*}$  ratio for SdI-2 is 28.9, which is much higher than is typical for UDGs irrespective of  $R_e$ , see Figure 5. As reported in Papastergis et al. (2017) this high  $\frac{M_{\text{HI}}}{M_*}$  ratio is consistent with the trend for isolated UDGs to show significantly higher  $\frac{M_{\text{HI}}}{M_*}$  ratios than UDGs in denser environments. It should be remembered that this plot only considers relatively isolated H I UDGs and does not include cluster galaxies which are expected to be H I deficient. That said we would expect the higher  $R_e$  region of the plot to favour high DM halo spin (Amorisco & Loeb 2016) or star formation SF driven extended disc (e.g. Di Cintio et al. 2017) formation models. Conversely, environment density driven formation scenarios should favour the lower  $M_{\text{HI}}/M_*$  ratio regions of the plot, but more H I observations of cluster galaxies are needed to explore this parameter space. A NED search revealed no companions projected within a radius of 30 arcmin ( $\sim 330$  kpc) and a velocity range of  $\pm 500$   $\text{km s}^{-1}$ . However, the SdI-2 head and tail H I morphology is suggestive of a recent interaction. Given this and that the nearest galaxy cluster (ZwCl 1141.7-0158B) is projected  $\sim 900$  kpc and  $-1055$   $\text{km s}^{-1}$  away, we can reasonably rule out ram pressure stripping as the origin of the one-sided H I tail. This leaves an interaction with a low mass satellite or gas cloud within  $7 \times 10^8$  yr as a likely explanation for the H I detached region. The above timescale is based on Holwerda et al. (2011), who predict the H I perturbations from even major mergers will only remain detectable in H I for a maximum of 0.4 to 0.7 Gyr. In summary the H I morphologies of both UDG-B1 and SdI-2 indicate a recent interaction.

The evidence for and against a recent interactions is discussed further in Section 4.2.

### 3.2 HI kinematics

Based on UDG-B1's GMRT H I spectrum, its  $V_{\text{HI}} = 6450 \pm 7$   $\text{km s}^{-1}$  and  $W_{20} = 90 \pm 15$   $\text{km s}^{-1}$ . This velocity agrees within the uncertainties with the  $V_{\text{HI}} = 6440 \pm 5$   $\text{km s}^{-1}$  and  $W_{50} = 50 \pm 10$   $\text{km s}^{-1}$  from the VLA (Spekkens & Karunakaran 2018). Figure 2 (top right panel) shows the UDG-B1 H I low resolution velocity field, with H I detected in the velocity range 6404  $\text{km s}^{-1}$  to 6512  $\text{km s}^{-1}$ . The H I velocity field shows a NE to W gradient, which indicates that the H I disc major axis is approximately perpendicular to the N – S optical axis and the change in the position angle of the iso-velocity contours from the NE to W suggests a warping of the disc, although with the caveat that the spatial resolution is low. We attempted to determine the rotational velocity ( $V_{\text{rot}}$ ) from a 3D model fit to the UDG-B1 H I emission in the medium resolution cube using BBAROLO (Di Teodoro & Fraternali 2015). Unfortunately, the small number of beams across the H I disc and the low signal to noise ratio (S/N) meant this attempt failed. Instead using inclination ( $i = 17.6^\circ$ ) and  $W_{20}$  derived from the medium resolution H I cube and equation 1 we estimated  $V_{\text{rot}} = 148$   $\text{km s}^{-1}$ .

$$v_{\text{rot}} = \frac{1}{2} \frac{W_{20}}{\sin(i)} \quad (1)$$

where,

$$\sin(i) = \sqrt{\frac{1 - \left(\frac{b}{a}\right)^2}{1 - q_0^2}}$$

a, b are the lengths of the major and minor H I axes, 43.3 arcsec and 41.46 arcsec respectively from the medium resolution H I map and  $q_0 = 0.3$  is the intrinsic axial ratio for an edge on galaxy (Sánchez-Janssen et al. 2010) and

$$W_{20} = \sqrt{w_{20\text{raw}}^2 - \delta_s^2}$$

where  $w_{20\text{raw}}$  is the  $W_{20}$  measured from the spectrum and  $\delta_s$  is a correction for instrumental broadening and turbulence (10  $\text{km s}^{-1}$ ).

However, this inclination corrected  $V_{\text{rot}}$  estimate of 148  $\text{km s}^{-1}$  is anomalously high by a factor of 2 to 3 for a UDG of its H I mass, even allowing for the significant uncertainties in the H I major and minor axes because synthesised beam is large relative to axes. So, as a check we also calculated  $V_{\text{rot}}$  using Equation 1 but replacing the H I axial ratio (b/a) with the optical axial ratio of 0.46 from Román & Trujillo (2017). This substitution resulted in a revised inclination of  $68.6^\circ$  and  $V_{\text{rot}} = 48$   $\text{km s}^{-1}$ . A visual assessment of the medium resolution H I map in Figure 1 indicates the H I axial ratio is significantly lower than its optical counterpart. It is also important to note the calculations above assume that the H I is dynamical equilibrium, but if UDG-B1 has suffered a recent interaction, as the analysis of the H I morphology suggests, the apparently large H I  $V_{\text{rot}}$  of 148  $\text{km s}^{-1}$  is more likely an interaction induced kinematic artefact rather than an usually large H I rotation velocity. The implications of the two  $V_{\text{rot}}$  estimates for calculation of UDG-B1's dynamical mass are discussed in section 4.1.

Measurement of SdI-2's GMRT H I spectrum gives  $V_{\text{HI}} = 2565 \pm 4$   $\text{km s}^{-1}$  and  $W_{20} = 80 \pm 6$   $\text{km s}^{-1}$ .  $V_{\text{HI}} = 2543$   $\text{km s}^{-1}$  and  $W_{50} = 69$   $\text{km s}^{-1}$  were reported for the galaxy in Papastergis et al. (2017) using observations from the Effelsberg 100 m telescope. SdI-2's velocity field in Figure 3 (lower right panel) shows two distinct

kinematic regions; the main HI body of the galaxy, which has a length of  $\sim 74''$  (14 kpc) and displays a regular velocity gradient indicating a possible rotating HI disc ( $\sim 2527 \text{ km s}^{-1}$  to  $2618 \text{ km s}^{-1}$ ) and a morphologically detached HI extension to the NE with a narrow range of velocities from  $\sim 2590 \text{ km s}^{-1}$  to  $2611 \text{ km s}^{-1}$ . HI velocities in the detached region are similar to those in NE of the main galaxy body. The systematic change in PA ( $\sim 90^\circ$ ) of the iso-velocity contours in the main body, indicates the HI disc is significantly warped. Based on the HI major and minor axes of the main body of the galaxy in medium resolution HI map we estimated the inclination of the HI disc at  $67^\circ$ . Using this inclination and  $W_{20}$  from the medium resolution SdI–2 cube and estimated  $V_{rot} = 41 \text{ km s}^{-1}$  using equation 1. We also attempted to use `BBAROLO` to fit a 3D model to the GMRT HI medium resolution cube which gave a fit with an inclination  $\sim 60^\circ$  and  $V_{rot} \sim 35 \text{ km s}^{-1}$ , but the low number of beams across the disc ( $\sim 3$ ) and low S/N ratio in the cube meant we could not place a strong reliance on the fit, but the inclination and  $V_{rot}$  from the two methods are in reasonable agreement. The PV diagram (Figure 4) is from a cut (PA =  $23.3^\circ$ ) oriented along the HI disc’s major axis. The PV diagram is consistent with a bulk of HI consisting of a rotating disc with the detached NE region only appearing in a narrow range of velocities ( $\sim 2590 \text{ km s}^{-1}$  to  $2611 \text{ km s}^{-1}$ ). Figure 4 also shows low level emission extending NE from main HI body toward the detached HI region and indicating the two HI structure are likely to be associated. This is discussed further in section 4.2.

## 4 DISCUSSION

### 4.1 Dark matter halos

Ideally a UDG’s dynamical mass would be determined using its HI rotation curve which in the field or in groups can probe a galaxy’s dynamical mass well beyond the radius of its stellar disk. By fitting a HI rotation curve to DM halo models the mass and mass profile of the DM halo can be estimated. But in clusters because of the absence of HI due to efficient HI stripping by the cluster environment, dynamical and DM halo mass estimates to date are typically based on globular cluster studies. (e.g. [Beasley & Trujillo 2016](#); [Beasley et al. 2016](#); [van Dokkum et al. 2018, 2019b,a](#)) This approach is supported by the scaling relation between the number of globular clusters and the host galaxy’s halo virial mass ([Burkert & Forbes 2020](#)), although the impact of the cluster on a UDGs globular population remain unclear ([Forbes et al. 2020a](#)). In the case of the Coma cluster UDG DF–44, which has the largest known DM halo mass of  $M_{200} = 10^{11} - 10^{12}$ , stellar kinematics provided the dynamical mass ([van Dokkum et al. 2019c](#)). There are a small number of Coma UDGs, like DF–44, which have high numbers of globular clusters per unit stellar mass implying extremely massive DM halos with two thirds of Coma UDGs ( $R_e > 1.5 \text{ kpc}$ ) having halo masses  $\geq 10^{11} M_\odot$  based on globular cluster–DM halo mass scaling relations [Forbes et al. \(2020a\)](#). These halo masses are consistent with the failed Milky Way mass galaxies. Earlier globular cluster-based studies of galaxy cluster UDGs had indicated that while high dynamical to stellar mass ratios were common, e.g. VCC 1287 and DF 17, typically those studies implied dwarf mass DM halos (e.g. [Beasley & Trujillo 2016](#); [Beasley et al. 2016](#)).

An important recent development has been reports of baryon dominated UDGs based on globular cluster studies ([van Dokkum et al. 2018, 2019b,a](#)) and resolved HI [Mancera Piña et al. \(2019, 2020\)](#). [Zaritsky \(2017\)](#), using scaling

relations, suggested that UDGs may span a range of DM halo masses between those typically found in large spirals to dwarf galaxies, but further observations are needed to confirm this. Deriving an accurate estimate of a UDG’s DM content from HI requires a rotation curve extracted from resolved HI observations. To date only a few UDGs have been mapped in HI (e.g. [Leisman et al. 2017](#); [Sengupta et al. 2019](#); [Mancera Piña et al. 2019](#)). Interestingly, several of these UDGs with resolved HI show an apparent departure from the [McGaugh et al. \(2000\)](#) baryonic Tully Fisher relation (BTFR). Analysis of the DM content of six of the UDGs in the Leisman sample of isolated HI detected UDGs ([Mancera Piña et al. 2019, 2020](#)) indicates that those galaxies are baryon dominated within their  $R_{HI}$ , see Figure 4 in [Mancera Piña et al. \(2019\)](#), although their results are based on a limited number of `BBAROLO` ([Di Teodoro & Fraternali 2015](#)) 3D kinematic tilted–ring disc model fits for each galaxy. A similar, although lower magnitude, departure from the BTFR was reported in [Sengupta et al. \(2019\)](#) for the UDG, UGC 2162 also derived from `BBAROLO` fitting. Confirmation of a baryon dominated population of UDGs has important implications for the origin of those UDGs. Additionally, the [Mancera Piña et al. \(2019, 2020\)](#) galaxies as well as UGC 2162 have a lower  $V_{rot}$  compared to normal dwarf galaxies of similar HI mass ([Mancera Piña et al. 2020](#); [Sengupta et al. 2019](#)). This is consistent with the results from the larger [Leisman et al. \(2017\)](#) sample which found the mean velocity width,  $W_{50}$ , for UDGs was significantly narrower ( $< 44 > \text{ km s}^{-1}$ ) than for ALFALFA galaxies with a similar selection criteria ( $< 119 > \text{ km s}^{-1}$ ).

As noted in section 3.2 the `BBAROLO` 3D kinematic tilted–ring disc models to the HI cube for UDG–B1 failed and for SdI–2 the fit provided only a poorly constrained estimate the DM halo properties. So as an alternative, we estimated their dynamical masses ( $M_{dyn}$ ) from the available HI properties. We did this using the HI radii from the medium resolution GMRT integrated HI maps for UDG–B1 and SdI–2 ( $\sim 4.0 \text{ kpc}$  and  $6.8 \text{ kpc}$  respectively) and their inclination corrected  $V_{rot}$   $148 \text{ km s}^{-1}$  (UDG–B1) and  $41 \text{ km s}^{-1}$  (SdI–2). Using this method their respective  $M_{dyn}$  was estimated at  $45.9 \times 10^9 M_\odot$  and  $2.7 \times 10^9 M_\odot$ . The baryonic masses ( $M_{baryon}$ ) of the galaxies ( $M_{HI} \times 1.4 + M_*$ ) from Table 2 equal  $1.76 \times 10^9 M_\odot$  and  $0.35 \times 10^9 M_\odot$  for UDG–B1 and SdI–2, respectively. The 1.4 factor applied to the HI masses was to adjust for the helium and molecular gas content of the UDGs. Based on these values the baryon fractions for UDG–B1 and SdI–2 are 0.05 and 0.14, respectively. These fractions indicate that, within the radii where HI was detected, both UDG–B1 and the main body of SdI–2 are both dark matter dominated.

However as noted in Section 3.2, the UDG–B1 inclination corrected  $V_{rot}$  estimate of  $148 \text{ km s}^{-1}$  derived from from the HI axial ratio is anomalously high. If instead we use  $V_{rot} = 48 \text{ km s}^{-1}$  based on the optical axial ratio it implies a  $M_{dyn} = 5.1 \times 10^9 M_\odot$  and baryon fraction ( $M_{bar} / M_{dyn}$ ) increases to 0.45. In figure 6, originally from [Mancera Piña et al. \(2020\)](#), we show the log of the ratio of baryonic to dynamical mass versus the log of dynamical mass for UDG–B1, SdI–2, and UGC 2162 ([Sengupta et al. 2019](#)) as well as the galaxies from the LITTLE THINGS ([Oh et al. 2015](#)), and [Mancera Piña et al. \(2019\)](#) as shown in [Mancera Piña et al. \(2020\)](#). For UDG– B1 we show the masses derived using both  $V_{rot} = 148 \text{ km s}^{-1}$  and  $48 \text{ km s}^{-1}$ , with a blue line joining the two sets of derived masses. The horizontal lines indicate the DM fraction ( $f_{DM}$ ) shown at the right–hand margin. For UDG–B1 the baryonic (or inversely DM) fraction depends on the adopted  $V_{rot}$  which in turn depends on whether the HI or optical axial ratio is used. Use of the

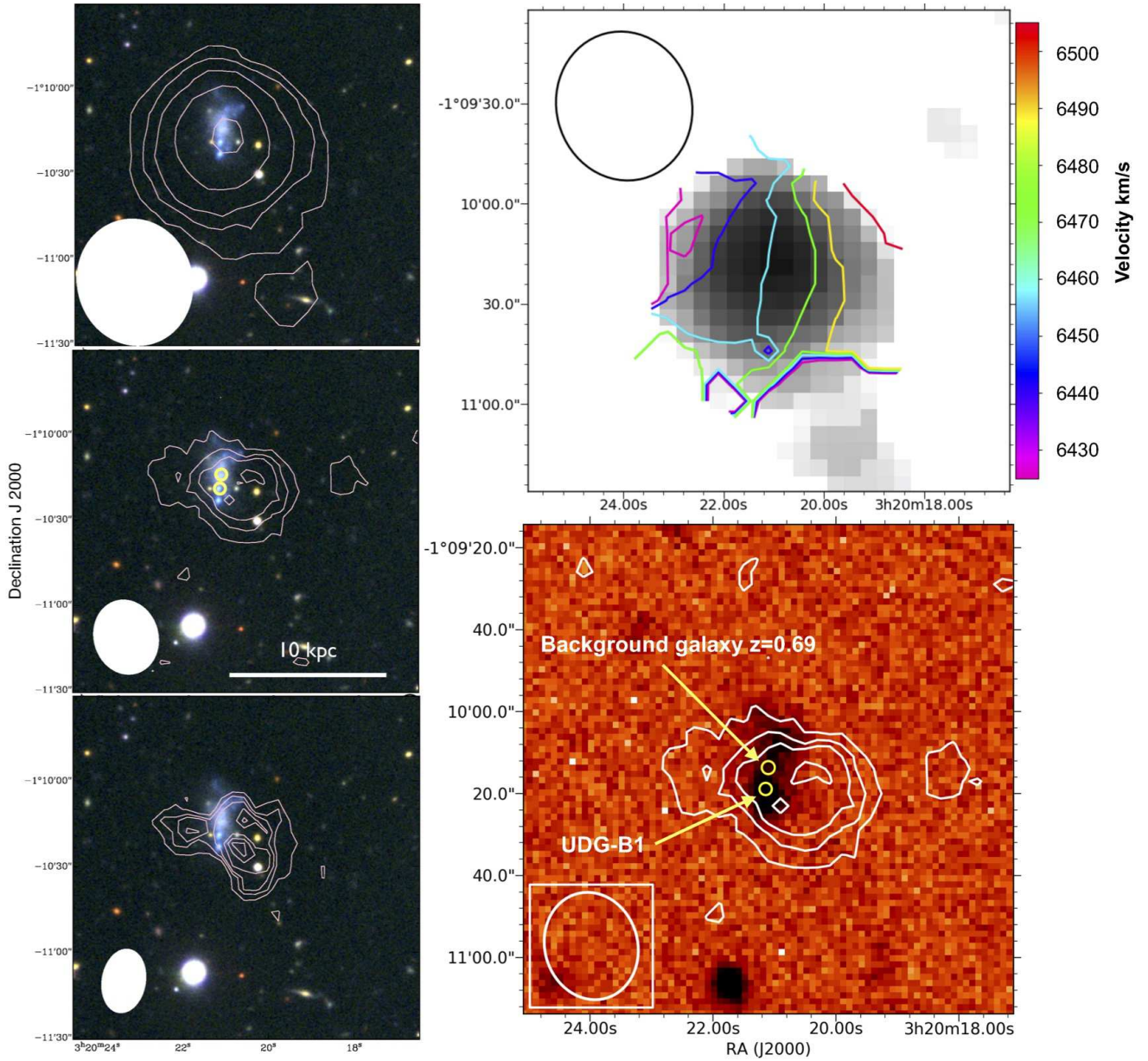


**Figure 2. UDG-B1: GMRT H I** *Left column (top to bottom):* Integrated H I contours from the low ( $44.82'' \times 40.48''$ ), medium  $26.46'' \times 22.65''$ ) and high ( $22.73'' \times 15.31''$ ) resolution maps overlaid on an IAC stripe 82 g, r, i composite images. The column density map contours are at, low resolution;  $0.39, 0.78, 1.17, 2.10$  and  $3.00 \times 10^{20}$  atoms  $\text{cm}^{-2}$ , medium resolution;  $1.46, 2.73, 3.6$  and  $5.5 \times 10^{20}$  atoms  $\text{cm}^{-2}$ , high resolution;  $1.26, 2.21, 2.84, 3.79, 4.74$  and  $5.60 \times 10^{20}$  atoms  $\text{cm}^{-2}$ . *Right top:* H I velocity field from the low resolution cube, with the iso-velocity contours values, separated by  $10 \text{ km s}^{-1}$ , indicated by the colour scale. *Lower right:* GMRT medium resolution ( $26.46'' \times 22.65''$ ) integrated H I map contours on a smoothed GALEX NUV image. The small yellow circles are the positions and fields of view of the two available SDSS spectra fibres. The ellipses in each panel indicates the size and orientation of the GMRT synthesized beams.

optical axial ratio implies  $V_{rot} = 48 \text{ km s}^{-1}$  and a baryon fraction of 0.45, which is close to that of the galaxy in the [Mancera Piña et al. \(2019\)](#) sample with the lowest baryon fraction. Alternatively, using the H I axes ratio and  $V_{rot} = 148 \text{ km s}^{-1}$  gives much lower baryon fraction of 0.05, which would place it near the extreme of DM dominated dwarfs. As observed in Section 3.2 there are reasons to think the  $V_{rot}$  values from which these baryonic fractions are derived are upper and lower limits. As a result we consider its likely that true

baryonic fraction of UDG-B1 lies at an intermediate point in range 0.05 to 0.45 and thus is likely be similar to the median value for the LITTLE THINGS dwarfs, see Figure 6.

Hence, in terms of DM content, our estimates of  $M_{dyn}$  for SdI-2, and the uncertainly for UDG-B1, suggest the DM halos within the H I radii resemble normal DM dominated dwarf galaxies. Figure 5 shows the  $M_{HI}/M_*$  v  $R_e$  for UDG-B1, SdI-2 and a selection of UDGs from the literature, including the baryon dominated UDGs

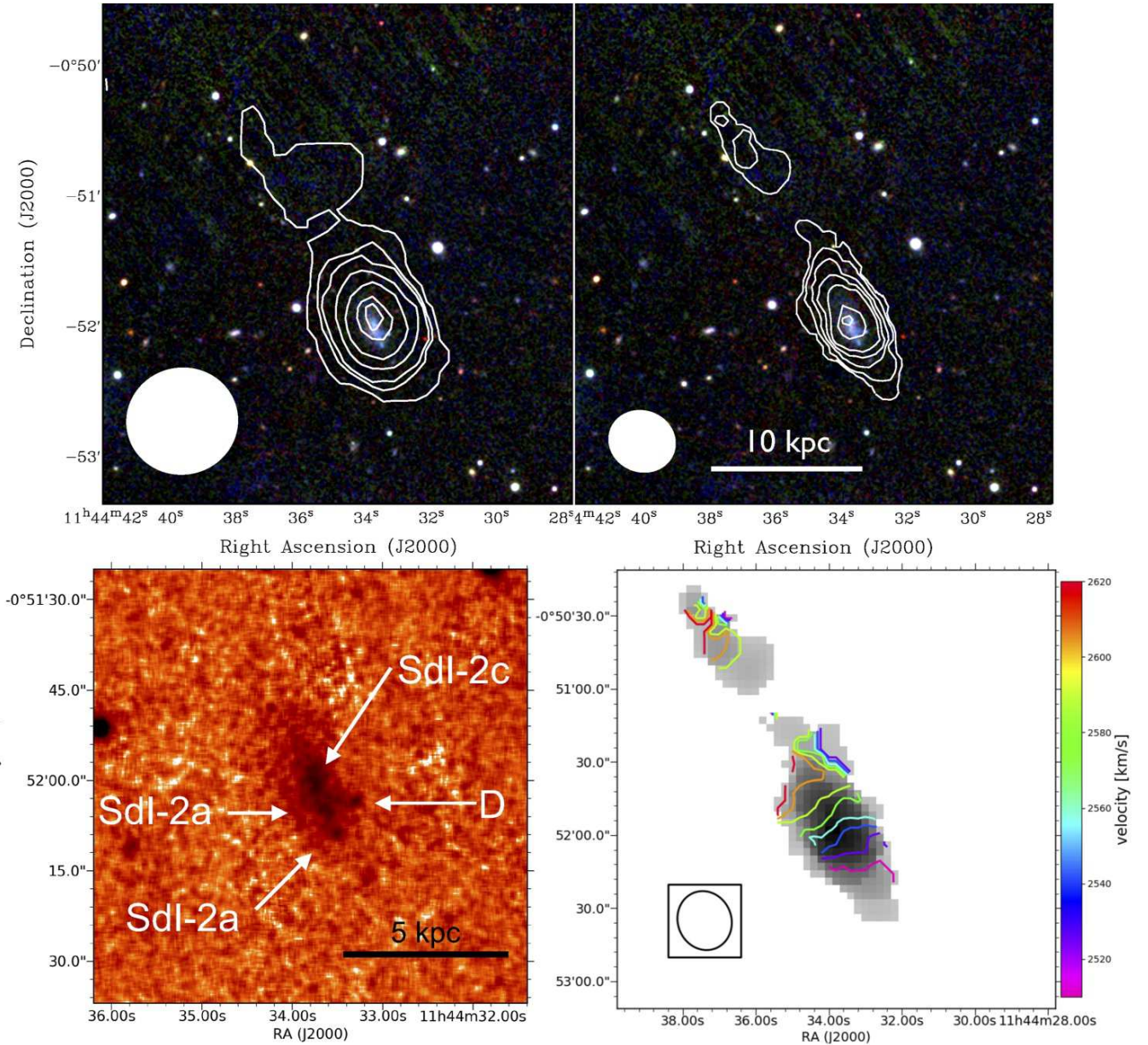


**Figure 3. SdI-2:** *Top (left to right):* GMRT low( $39.95'' \times 35.38''$ ) and medium ( $24.50'' \times 21.99''$ ) resolution HI contours overlaid on a Pan-STARRS g,r,i-band composite image. The column density map contours are at, low resolution;  $0.15, 0.54, 0.77, 1.55, 2.33, 3.11$  and  $3.50 \times 10^{20}$  atoms  $\text{cm}^{-2}$ , medium resolution;  $0.40, 1.02, 1.83, 3.06, 4.08, 6.10$  and  $7.14 \times 10^{20}$  atoms  $\text{cm}^{-2}$ . *Lower left:* SdI-2 smoothed NUV (GALEX) image with the star forming regions from Bellazzini et al. (2017) indicated. *Lower right:* Medium resolution HI velocity field iso-velocity contours separated by  $10 \text{ km s}^{-1}$  overlaid on HI integrated medium resolution map. The GMRT beam sizes and orientations are shown with ellipses at the bottom of each panel.

reported in (Mancera Piña et al. 2019, 2020), which have  $R_e \gtrsim 3$  kpc.  $R_e$  and their uncertainties in the plot are from the literature sources, principally from Leisman et al. (2017) which are based on their own photometry of SDSS images. We note from the Figure that UDG-B1 has a  $R_e$  within the  $R_e$  range where baryon dominated UDGs have been reported. This suggests that for UDGs outside clusters their  $R_e$  is determined by factor other than their baryon fraction and  $\frac{M_{\text{HI}}}{M_*}$  ratio.

#### 4.2 Evidence for ongoing interactions

Figure 2 (left middle panel) shows the IAC stripe 82 optical image of the UDG-B1 and the two small over plotted yellow circles indicate the positions and 3 arcsec diameters of the SDSS spectra fibres. Each spectra is from a different galaxy with the spectrum in the south from UDG-B1 and the one above it from a background galaxy. With the aid of the SDSS spectra and a NUV (GALEX) image (Figure 2 – lower right panel) we interpret the optical image as

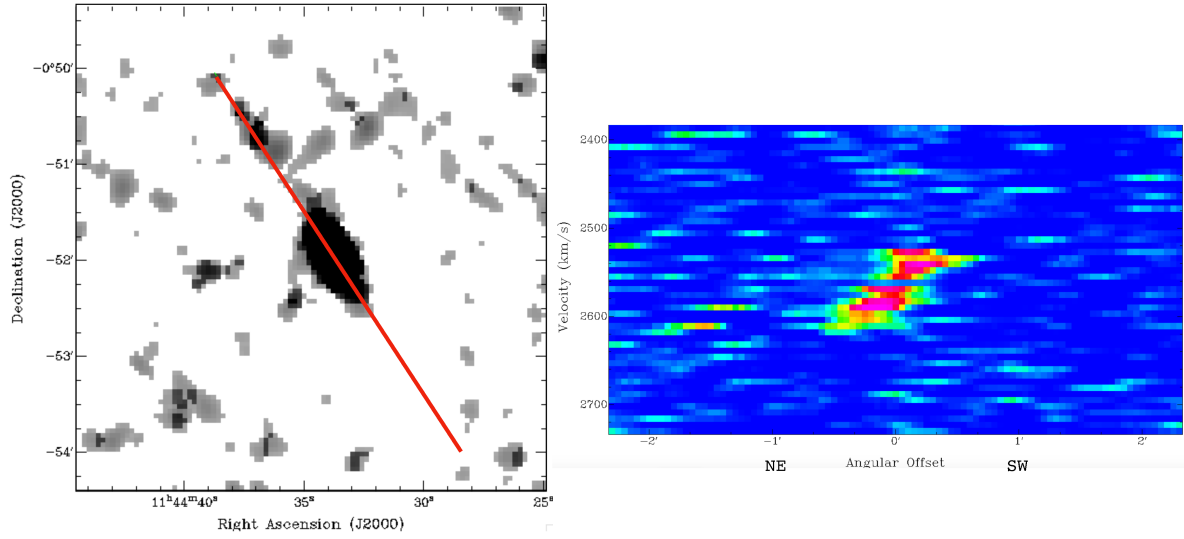


**Figure 4. SdI-2 PV diagram:** from the low resolution GMRT cube (spatial resolution  $\sim 40$  arcsec). The cut (PA  $23.3^\circ$ ) is through the centre along the major HI axis. Positive angular offsets are to the SW of the optical centre and negative offsets are to the NE and include the HI NE detached feature. The velocity resolution of the cube is  $7 \text{ km s}^{-1}$ .

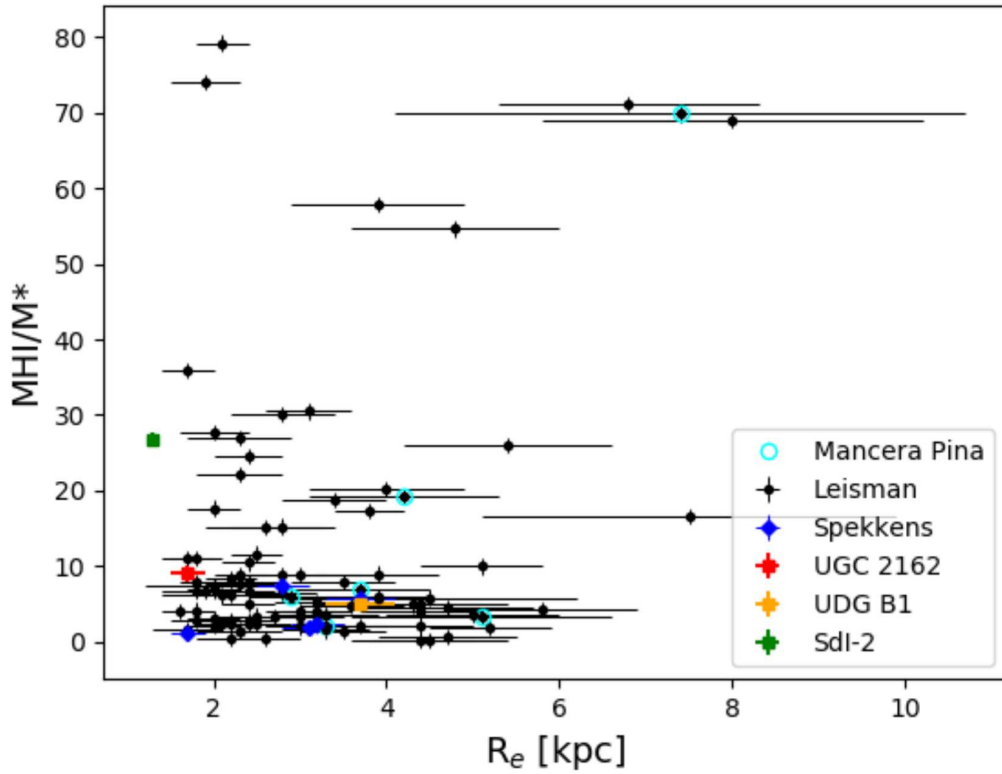


**Figure 5.  $M_{\text{HI}} / M_*$  v  $R_e$  for UDG-B1, SdI-2 and selected UDGs reported in the literature i.e. from Mancera Piña et al. (2019, 2020), Leisman, et al., (2017), Spekkens & Karunakaran (2018), Sengupta et al. (2019.)**

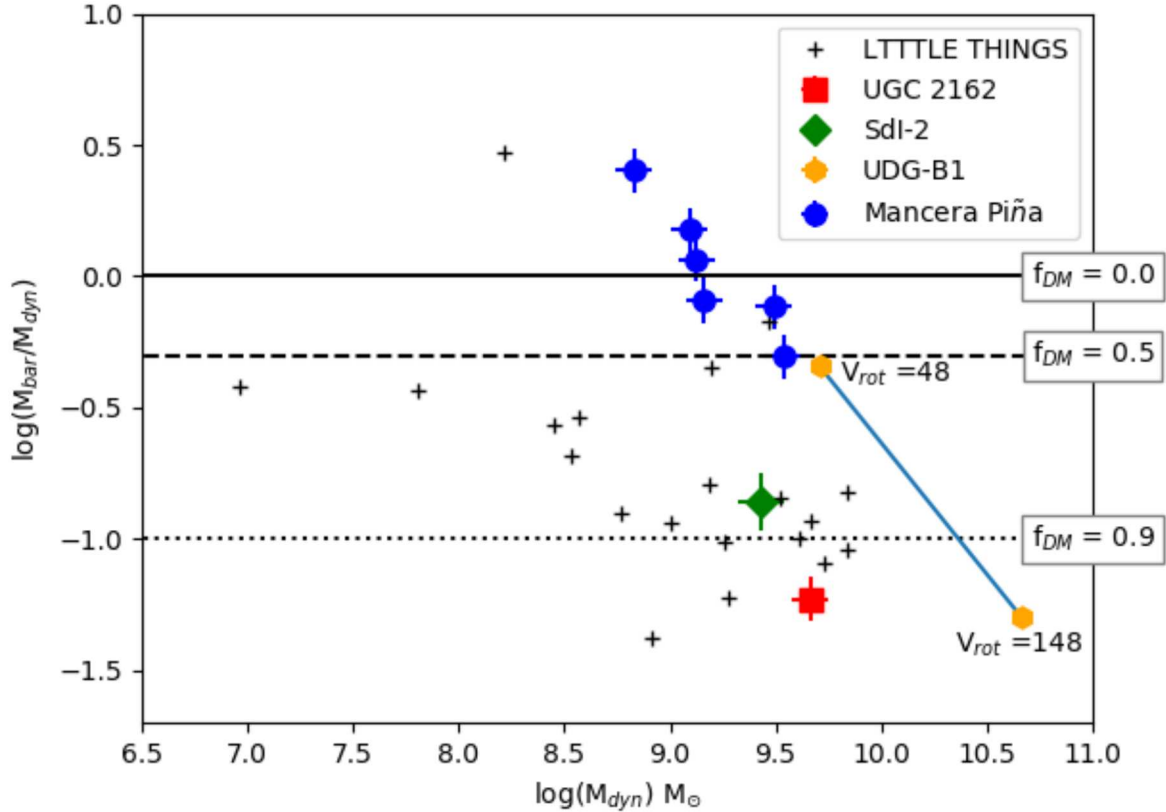


**Figure 6.**  $M_{\text{bar}} / M_{\text{dyn}} \nu M_{\text{dyn}}$ : for UDG–B1 and SdI–2 in comparison to the UDG samples from Mancera Piña et al., (2020), dwarf galaxies LITTLE THINGS (Oh et al. 2015) and UDG 2162 (Sengupta et al. 2019.). For UDG B1 we show the  $M_{\text{dyn}}$  determined using the two values  $V_{\text{rot}}$ , 48  $\text{km s}^{-1}$  and 148  $\text{km s}^{-1}$  discussed in Section 3.2. The blue line indicates the range these two values cover. The horizontal lines indicate the dark matter fractions shown in right hand margin.

showing that UDG–B1 is projected in front of a  $z=0.69010 \pm 0.0005$  background galaxy and extends in faint blue emission  $\sim 30$  arcsec (12.5 kpc) north of the strong star forming region detected in the SDSS UDG–B1 spectrum. This picture of UDG–B1’s elongated N–S morphology is confirmed by the GALEX NUV emission in Figure 2 – lower left panel.

From the UDG–B1 GMRT medium and high resolution HI maps we see the high column density HI is located W of the optical/NUV axes (Figure 2). UDG–B1’s  $R_e$  is 3.7 kpc (Román & Trujillo 2017) and the NED major optical axis of 0.35 arcmin indicates the  $R_{\text{opt}}$  is  $\sim 4.4$  kpc. Based on the first order 43.3 arcsec major axis estimate from medium resolution HI map we estimate the  $R_{\text{HI}}$  at 9 kpc and the  $R_{\text{HI}}/R_{\text{opt}}$  ratio = 2.0. So even allowing for the asymmetric nature of the HI distribution and uncertain inclination the UDG–B1  $R_{\text{HI}}/R_{\text{opt}}$  ratio is consistent with the typical  $R_{\text{HI}}/R_{\text{opt}}$  of 1.8 for late type galaxies (Broeils & Rhee 1997), i.e., we see no clear indication that the UDG–B1 HI disc is truncated.

The low resolution HI velocity field for UDG–B1 (Figure 2 – upper right panel) shows an overall rotation pattern running approximately perpendicular to the optical/NUV axes, but the change in iso-velocity angle from NE to W suggesting a possible warped disc. The HI/optical axis offset, HI warp and anomalous  $V_{\text{rot}}$  are all signatures of an interaction well within the HI relaxation time scale of  $<0.7$  Gyr (Holwerda et al. 2011). Such an interaction is likely

to have been with a member of HCG 25 group. As noted in Section 3.1 the medium and high-resolution HI maps show the current blue star-forming region is offset in projection from the HI column density maxima which could be a further signature of a recent tidal interaction. A galaxy’s  $A_{\text{flux}}$  ratio is a measure of the asymmetry in its integrated HI flux density profile (within its  $W_{20}$  velocity range) at velocities above and below the galaxy’s systemic velocity ( $V_{\text{HI}}$ ).  $A_{\text{flux}} = 1.00$  is a perfectly symmetric spectrum and  $A_{\text{flux}} > 1.26$  presents a clear asymmetry signature (Espada et al. 2011; Scott et al. 2018; Reynolds et al. 2020). The  $A_{\text{flux}}$  for UDG–B1 is  $1.23 \pm 0.11$  providing only marginal support for a recent interaction, particularly in because low signal to noise is understood to increase  $A_{\text{flux}}$  values (Watts et al. 2020).

UDG–B1’s SDSS spectrum cannot be considered representative of the galaxy as a whole because of the 3 arcsec diameter the SDSS spectrum fibre samples only  $\sim 2.6\%$  of the UDG–B1 optical  $R_e$  disc area and this region has a bluer color than the rest of the galaxy (Román & Trujillo 2017). Measurements derived from the spectrum, including oxygen abundance,  $<12+\log(\text{O}/\text{H})> = 8.01 \pm 0.39$ , and  $\text{SFR}(\text{H}\alpha) \sim 0.0033 M_{\odot} \text{ yr}^{-1}$  are set out in Table 3. In this table  $<12+\log(\text{O}/\text{H})>$  was obtained as the average from the Marino et al. (2013), (Kobulnicky et al. 1999, lower branch) and Pettini & Pagel (2004) calibrators. The starformation rate was calculated assuming the Kennicutt (1998) conversion formula af-

**Table 3.** UDG-B1: Emission line fluxes and properties from the SDSS spectrum. The average  $12 + \log(\text{O}/\text{H})$  is obtained from the Marino et al. (2013), Kobulnicky et al. (1999; lower branch) and Pettini & Pagel (2004) calibrators, respectively.

$I(\lambda)/I(\text{H}\beta) \times 100$	
[SII]6731	257.08 $\pm$ 8.41
[SII]6717	95.64 $\pm$ 3.85
[NII]6584	3.88 $\pm$ 0.09
H $\alpha$	177.78 $\pm$ 5.59
[OIII]5007	257.08 $\pm$ 8.41
[OIII]4959	95.64 $\pm$ 3.85
H $\beta$	100.00 $\pm$ 4.47
[OII]3727	253.08 $\pm$ 14.54
<hr/>	
F(H $\alpha$ ) $\times 10^{-16}$ erg cm $^{-2}$ s $^{-1}$	7.72 $\pm$ 0.07
F(H $\beta$ ) $\times 10^{-16}$ erg cm $^{-2}$ s $^{-1}$	4.34 $\pm$ 0.10
H $\alpha$ /H $\beta$ $\times 100$	177.78 $\pm$ 0.06
c(H $\beta$ )	0.00 $\pm$ 0.03
EW(H $\alpha$ ) $\text{\AA}$	115.0
EW(H $\beta$ ) $\text{\AA}$	41.0
<hr/>	
log([OIII]/H $\beta$ )	0.41 $\pm$ 0.03
log([NII]/H $\alpha$ )	-1.66 $\pm$ 0.04
log([SII]/H $\alpha$ )	-0.53 $\pm$ 0.09
<hr/>	
SFR(H $\alpha$ ) $M_{\odot}$ yr $^{-1}$	0.003 $\pm$ 0.001
M(HII) $\times 10^5 M_{\odot}$	1.71
$12 + \log(\text{O}/\text{H})_M$	7.98 $\pm$ 0.19
$12 + \log(\text{O}/\text{H})_{KL}$	7.97 $\pm$ 0.26
$12 + \log(\text{O}/\text{H})_{PP}$	8.07 $\pm$ 0.22
$\langle 12 + \log(\text{O}/\text{H}) \rangle$	8.01 $\pm$ 0.39

ter correction for Chabrier IMF. The spectrum was corrected for galactic extinction and internal extinction was insignificant. The sub-solar  $12 + \log(\text{O}/\text{H})$  values for UDG-B1 indicate that the gas, at least at the position of the spectrum, is unlikely to have been acquired from more evolved members of HCG 25. Additionally, analysis of the SDSS spectra by Román & Trujillo (2017) indicates a stellar age  $< 0.1$  Gyr for the region within the SDSS fibre. This young stellar age may simply reflect a local stochastic increase in UDG-B1s star formation, but presence of H I perturbation signatures make it more likely the recent enhancement of SF was triggered by an interaction. In summary the UDG-B1 H I morphology and kinematics both show indications of a recent interaction, which has perturbed its H I disc, most likely with another member of HCG 25 and the blue color and young age of the stellar population at the position of the SDSS spectrum is consistent with star formation triggered by the interaction.

SdI-2's two most striking features are its high  $M_{\text{HI}}/M_*$  ratio of 28.9 (see Figure 5), which is comparable to the well known extremely gas-rich dwarf DDO 154 ( $M_{\text{HI}}/M_* = 31$  Watts et al. 2018), and its detached H I extended NE region (Figure 3). Given SdI-2's isolation, ram pressure stripping can almost certainly be ruled out as an explanation for the SdI-2 detached H I extension. So, the most likely explanation for the detached H I extension is that it is debris from the accretion of a smaller gas-rich satellite. There are examples in the literature of isolated galaxies with one-sided H I tails and warped discs attributed to the accretion of or interactions with satellite galaxies (Martínez-Delgado et al. 2009; Sengupta et al. 2012; Scott et al. 2014). However, this proposition is only marginally supported by analysis of the integrated GMRT H I spectrum profile,  $A_{\text{flux}} = 1.20 \pm 0.07$ . While the evidence from the H I profile analysis is inconclusive, the resolved integrated H I maps and velocity

field maps (from the medium resolution cube) provide signatures characteristic of a recent interaction. This demonstrates the higher sensitivity to recent H I interactions of resolved mapping compared to H I profile analysis.

Figure 3, lower left panel, shows a smoothed NUV (GALEX) image of SdI-2. SDSS catalogues the clump marked 'D' in the figure as a star but it could alternatively be a background galaxy. Optically, SdI-2 consists of an elongated region of bright starforming clumps oriented approximately N-S. Three of these clumps, SdI-2-a, SdI-2-b and SdI-2-c are identified in the Figure using the nomenclature from Bellazzini et al. (2017). These bright clumps are surrounded by a larger region of low surface brightness NUV emission (Figure 3). This low surface brightness emission is more extended in the NE, extending  $\sim 20$  arcsec (3.6 kpc) NE of the optical centre. Bellazzini et al. (2017) reported  $12 + \log(\text{O}/\text{H})$  of  $8.1 \pm 0.02$  for clumps SdI-2-a and SdI-2-b, with the difference between them being indistinguishable within the errors. Those authors also reported on a spectrum from the optical centre, SdI-2-c, with model fits indicating a stellar metallicity of  $Z=0.002$  and age of 200 Myr. This spectrum differed from SdI-2-a and SdI-2-b in not having any significant emission lines, presumably because of a lack of ionising photons. The SdI-2-c  $\log(\text{N}/\text{O})$  from Bellazzini et al. (2017) is -1.7 implying a primary production of nitrogen in a low metallicity environment. However, the observed uncertainties of N/O at  $12 + \log(\text{O}/\text{H}) \lesssim 8.3$  has been attributed in the literature to a loss of heavy elements via a strong burst (galactic winds) in the recent past or because of the delayed production of oxygen and nitrogen by massive and intermediate-mass stars assuming a low star formation efficiency. So, a possible explanation of the lack of emission line in the SdI-2-c spectrum and the NUV halo is a recent strong burst of SF, but the difficulty with this scenario is the absence of the massive star clusters ( $M^* \sim 10^4 M_{\odot}$ ) this burst should have produced. We, therefore, conclude that the brightest observed starforming clumps are unlikely to be the result of strong recent star burst. SdI-2's H I morphology, together with its regular rotating, but wrapped, main body H I disc as well as the perturbed H I kinematics in the NE of the main H I body at similar velocities to those in the detached H I extension (Figure 3 Lower right panel) are suggestive of a recent tidal interaction. While, SdI-2-a and SdI-2-b could be remnants of an absorbed satellite or star forming regions triggered by such an interaction we do not have definitive proof of this.

## 5 SUMMARY AND CONCLUDING REMARKS

We report on H I mapping using the GMRT for two ultra-diffuse galaxies (UDGs) from contrasting environments. UDG-B1 is projected  $\sim 225$  kpc SW of the compact group HCG 25 while SeccodI-2 (SdI-2) is a relatively isolated UDG. These two UDGs also have contrasting effective radii with  $R_e$  of 3.7 kpc (similar to the Milky Way) and 1.3 kpc respectively. The H I morphology and kinematics of UDG-B1 suggest a recent interaction has perturbed both the morphology and kinematics of its H I. UDG-B1's subsolar metallicity suggests it did not acquire a significant gas mass in the interaction. SdI-2 has two striking features, first its  $\frac{M_{\text{HI}}}{M_*}$  ratio is 28.9 and despite its isolation, it displays a one-sided detached extended H I region to the NW. Its  $\frac{M_{\text{HI}}}{M_*}$  ratio implies a very low historic star formation efficiency. Based on our estimate of  $M_{\text{dyn}}$  the baryon fraction within H I radius for SdI-2 is 0.14, indicating that galaxy is dark matter dominated, at least within the radius in which H I is detected. However, the baryon fraction for UDG-B1 is quite

uncertain because of large uncertainties about the HI disc's inclination and the question as to whether its HI is in dynamical equilibrium. As a result we were unable to reliably estimate the UDG–B1 DM fraction. The higher  $M_{\text{HI}}/M_*$  ratio in SdI–2 compared to UDG–B1 is consistent with the result from Papastergis et al. (2017) which indicated UDGs further from group centres have higher  $M_{\text{HI}}/M_*$  ratios. In the case of UDG–B1 morphological evidence of tidal disturbance and possible stripping (and possibly ram pressure stripping) could explain the smaller stellar mass and redder colour of UDGs at distances closer to group centres as reported in Papastergis et al. (2017). Our study highlights the importance of high spatial and spectral resolution HI observations for the study of the dark matter properties of UDGs. While the narrow range of HI velocities in UDGs argues for a velocity resolution below  $\sim 10 \text{ km s}^{-1}$ , going beyond this level also requires good signal to noise, which adds a further burden to already demanding observations.

## ACKNOWLEDGEMENTS

We thank the staff of the *GMRT* who have made these observations possible. The *GMRT* is operated by the National Centre for Radio Astrophysics of the Tata Institute of Fundamental Research. TS acknowledge support by Fundação para a Ciência e a Tecnologia (FCT) through national funds (UID/FIS/04434/2013), FCT/MCTES through national funds (PIDDAC) by this grant UID/FIS/04434/2019 and by FEDER through COMPETE2020 (POCI-01-0145-FEDER-007672). TS also acknowledges the support by the fellowship SFRH/BPD/103385/2014 funded by the FCT (Portugal) and POPH/FSE (EC). TS additionally acknowledges support from DL 57/2016/CP1364/CT0009 from The Centro de Astrofísica da Universidade do Porto. PL is supported by a work contract DL 57/2016/CP1364/CT0010 funded by the FCT. This work was supported by FCT/MCTES through national funds (PIDDAC) by this grant PTDC/FIS-AST/29245/2017. Support for this work was provided by the National Research Foundation of Korea to the Center for Galaxy Evolution Research (No. 2010-0027910) and NRF grant No. 2018R1D1A1B07048314. This research has made use of the NASA/IPAC Extragalactic Database (NED) which is operated by the Jet Propulsion Laboratory, California Institute of Technology, under contract with the National Aeronautics and Space Administration. This research has made use of the Sloan Digital Sky Survey (SDSS). Funding for the SDSS and SDSS-II has been provided by the Alfred P. Sloan Foundation, the Participating Institutions, the National Science Foundation, the U.S. Department of Energy, the National Aeronautics and Space Administration, the Japanese Monbukagakusho, the Max Planck Society, and the Higher Education Funding Council for England. The SDSS Web Site is <http://www.sdss.org/>. This research made use of APLpy, an open-source Python plotting package hosted at <http://aplpy.github.com>, (Robitaille & Bressert 2012).

## DATA AVAILABILITY

The data underlying this article will be shared on reasonable request to the corresponding author.

## REFERENCES

Amorisco N. C., Loeb A., 2016, *MNRAS*, **459**, L51

- Baars J. W. M., Genzel R., Pauliny-Toth I. I. K., Witzel A., 1977, *A&A*, **61**, 99
- Baushev A. N., 2016, *J. Cosmology Astropart. Phys.*, **2016**, 018
- Beasley M. A., Trujillo I., 2016, *ApJ*, **830**, 23
- Beasley M. A., Romanowsky A. J., Pota V., Navarro I. M., Martinez Delgado D., Neyer F., Deich A. L., 2016, *ApJ*, **819**, L20
- Bellazzini M., Belokurov V., Magrini L., Fraternali F., Testa V., Beccari G., Marchetti A., Carini R., 2017, *MNRAS*, **467**, 3751
- Borthakur S., Yun M. S., Verdes-Montenegro L., 2010, *ApJ*, **710**, 385
- Broeils A. H., Rhee M.-H., 1997, *A&A*, **324**, 877
- Burkert A., Forbes D. A., 2020, *AJ*, **159**, 56
- Carleton T., Errani R., Cooper M., Kaplinghat M., Peñarrubia J., 2018, 2018arXiv180506896C,
- Conselice C. J., 2018, *Research Notes of the American Astronomical Society*, **2**, 43
- Di Cintio A., Brook C. B., Dutton A. A., Macciò A. V., Obreja A., Dekel A., 2017, *MNRAS*, **466**, L1
- Di Teodoro E. M., Fraternali F., 2015, *MNRAS*, **451**, 3021
- Espada D., Verdes-Montenegro L., Huchtmeier W. K., Sulentic J., Verley S., Leon S., Sabater J., 2011, *A&A*, **532**, A117
- Flewelling H. A., et al., 2016, arXiv e-prints, [p. arXiv:1612.05243](https://arxiv.org/abs/1612.05243)
- Forbes D. A., Alabi A., Romanowsky A. J., Brodie J. P., Arimoto N., 2020a, *MNRAS*, **492**, 4874
- Forbes D. A., Dullo B. T., Gannon J., Couch W. J., Iodice E., Spavone M., Cantiello M., Schipani P., 2020b, *MNRAS*, **494**, 5293
- Guo Q., et al., 2020, *Nature Astronomy*, **4**, 246
- Holwerda B. W., Pirzkal N., Cox T. J., de Blok W. J. G., Weniger J., Bouchard A., Blyth S.-L., van der Heyden K. J., 2011, *MNRAS*, **416**, 2426
- Janssens S. R., Abraham R., Brodie J., Forbes D. A., Romanowsky A. J., 2019, *ApJ*, **887**, 92
- Kennicutt Robert C. J., 1998, *ApJ*, **498**, 541
- Kobulnicky H. A., Kennicutt Robert C. J., Pizagno J. L., 1999, *ApJ*, **514**, 544
- Koda J., Yagi M., Yamanoi H., Komiyama Y., 2015, *ApJL*, **807**, L2
- Lagos P., Telles E., Nigoche-Netro A., Carrasco E. R., 2011, *AJ*, **142**, 162
- Leisman L., et al., 2017, *ApJ*, **842**, 133
- Liao S., et al., 2019, *MNRAS*, **490**, 5182
- Mancera Piña P. E., et al., 2019, arXiv e-prints, [p. arXiv:1909.01363](https://arxiv.org/abs/1909.01363)
- Mancera Piña P. E., et al., 2020, ArXiv 180404139L, [p. arXiv:2004.14392](https://arxiv.org/abs/2004.14392)
- Marino R. A., et al., 2013, *A&A*, **559**, A114
- Martínez-Delgado D., Pohlen M., Gabany R. J., Majewski S. R., Peñarrubia J., Palma C., 2009, *ApJ*, **692**, 955
- McGaugh S. S., Schombert J. M., Bothun G. D., de Blok W. J. G., 2000, *ApJL*, **533**, L99
- Oh S.-H., et al., 2015, *AJ*, **149**, 180
- Papastergis E., Adams E. A. K., Romanowsky A. J., 2017, *A&A*, **601**, L10
- Pettini M., Pagel B. E. J., 2004, *MNRAS*, **348**, L59
- Reynolds T. N., Westmeier T., Staveley-Smith L., Chauhan G., Lagos C. D. P., 2020, *MNRAS*, **493**, 5089
- Robitaille T., Bressert E., 2012, APLpy: Astronomical Plotting Library in Python, Astrophysics Source Code Library (ascl:1208.017)
- Román J., Trujillo I., 2017, *MNRAS*, **468**, 4039
- Sánchez-Janssen R., Méndez-Abreu J., Aguerri J. A. L., 2010, *MNRAS*, **406**, L65
- Scott T. C., et al., 2014, *A&A*, **567**, A56
- Scott T. C., Brinks E., Cortese L., Boselli A., Bravo-Alfaro H., 2018, *MNRAS*, **475**, 4648
- Sengupta C., et al., 2012, *A&A*, **546**, A95
- Sengupta C., Scott T. C., Chung A., Wong O. I., 2019, *MNRAS*, **488**, 3222
- Spekkens K., Karunakaran A., 2018, *ApJ*, **855**, 28
- Springob C. M., Haynes M. P., Giovanelli R., Kent B. R., 2005, *ApJS*, **160**, 149
- Tanoglidis D., et al., 2020, ArXiv 180404139L, [p. arXiv:2006.04294](https://arxiv.org/abs/2006.04294)
- Tovmassian H. M., Martínez O., Tiersch H., 1999, *A&A*, **348**, 693
- Trujillo I., Roman J., Filho M., Sánchez Almeida J., 2017, *ApJ*, **836**, 191
- Wang J., Yang K., Zhang Z.-Y., Fang M., Shi Y., Liu S., Li J., Li F., 2020, *MNRAS*, **499**, L26

- Watts A. B., Meurer G. R., Lagos C. D. P., Bruzese S. M., Kroupa P., Jerabkova T., 2018, *MNRAS*, **477**, 5554
- Watts A. B., Catinella B., Cortese L., Power C., 2020, *MNRAS*, **492**, 3672
- Yagi M., Koda J., Komiyama Y., Yamanoi H., 2016, *ApJS*, **225**, 11
- Yozin C., Bekki K., 2015, *MNRAS*, **452**, 937
- Zaritsky D., 2017, *MNRAS*, **464**, L110
- van Dokkum P. G., Abraham R., Merritt A., Zhang J., Geha M., Conroy C., 2015, *ApJL*, **798**, L45
- van Dokkum P., et al., 2018, *Nature*, **555**, 629
- van Dokkum P., Danieli S., Romanowsky A., Abraham R., Conroy C., 2019a, *Research Notes of the American Astronomical Society*, **3**, 29
- van Dokkum P., Danieli S., Abraham R., Conroy C., Romanowsky A. J., 2019b, *ApJL*, **874**, L5
- van Dokkum P., et al., 2019c, *ApJ*, **880**, 91
- van der Burg R. F. J., et al., 2017, *A&A*, **607**, A79

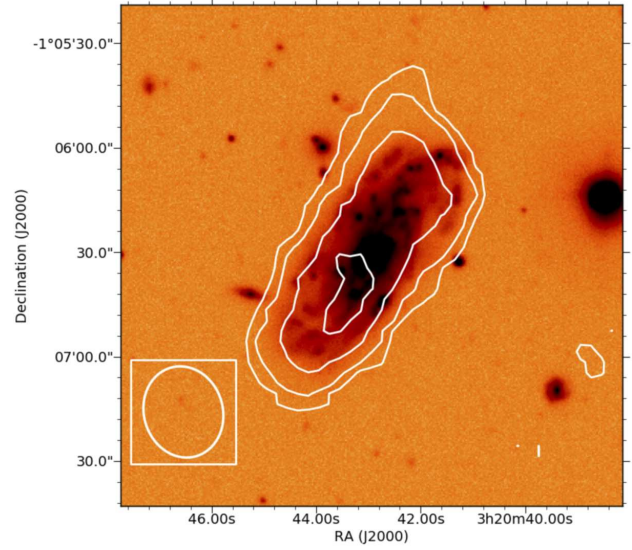


**Figure 7.** UGC 2690: GMRT medium resolution ( $26.46'' \times 22.65''$ ) H I velocity integrated map contours on Stripe 82 SDSS *g*-band image. The contours are at  $2.3, 4.6, 9.2$  and  $13.8 \times 10^{20}$  atoms  $\text{cm}^{-2}$ . The GMRT beam size and orientation is shown with white ellipse at the bottom left of the figure.

## APPENDIX A

### UGC 2690

H I was also detected in the SAc galaxy UGC 2690, within GMRT UDG B1 field of view, at  $V_{\text{HI}} = 6275 \pm 4 \text{ km s}^{-1}$  with  $W_{20} = 340 \pm 8 \text{ km s}^{-1}$ . The H I morphology from the medium resolution cube is shown in Figure 7 and displays an asymmetric increase in minor axis diameter NE of the optical centre. A similar asymmetry is seen in optical image. It seems likely both the H I and optical features are due to a recent interaction with another group member. The  $V_{\text{HI}} = 6269 \pm 2 \text{ km s}^{-1}$  and  $W_{20} = 340 \pm 8 \text{ km s}^{-1}$  from the GBT spectrum (Springob et al. 2005) agree within the uncertainties to the GMRT values. Measured from the GMRT spectrum the  $A_{\text{flux}} = 1.22 \pm 0.09$  and  $\Delta_{\text{sys}}$ , as defined by Reynolds et al. (2020), =  $5.3 \pm 6$ . As was the case for SdI-2 the resolved mapping is more sensitive to indications of perturbation than the H I profile parameters. Figure 8 shows the BBAROLO velocity field, data, model and residuals from the medium resolution cube and the PV diagram (PA =  $128^\circ$ ) for UGC 2690. The BBAROLO model fit indicates an H I  $V_{\text{rot}} = 150 \text{ km s}^{-1} \sim$  inclination of  $\sim 79^\circ$ .

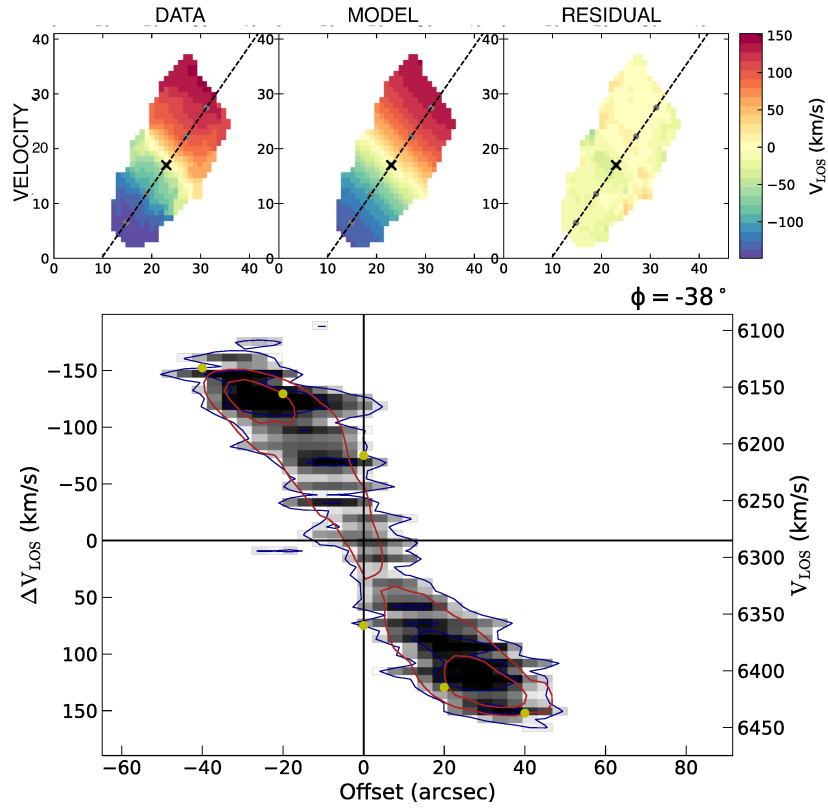


**Figure 8. UGC 2690:** top: BBAROLO data, model and residual from the medium resolution ( $26.46'' \times 22.65''$ ) GMRT HI cube. Bottom: BBAROLO PV diagram for PA =  $128^\circ$  from the same cube. The blue contours are from the data and the red contours are from the model, with the yellow dots showing the fitted rings.